Available online at www.sciencedirect.com
SCIENCE DIRECT®
Journal of Power Sources 119–121 (2003) 161–165
JOURNAL OF POWER SOURCES
www.elsevier.com/locate/jpowsour

Synthesis and electrochemical properties of layered $Li[Li_{0.15}Ni_{(0.275-x/2)}Al_xMn_{(0.575-x/2)}]O_2$ materials prepared by sol–gel method

Sang Ho Park, Yang-Kook Sun*

Department of Chemical Engineering, College of Engineering, Hanyang University, Seoul 133-791, South Korea

Abstract

Layered $Li[Li_{0.15}Ni_{(0.275-x/2)}Al_xMn_{(0.575-x/2)}]O_2$ materials were synthesized via a sol–gel method at 900 °C in air. $Li[Li_{0.15}Ni_{(0.275-x/2)}Al_xMn_{(0.575-x/2)}]O_2$ and Li_2MnO_3 phase mixed compounds were obtained. Substitution of Al^{3+} ions were shown to prevent the structural degradation of the electrode material allowing higher discharge capacities. The 6 mol% aluminum-doped $Li[Li_{0.15}Ni_{0.245}Al_{0.06}Mn_{0.545}]O_2$ electrode delivered approximately 210 mAh g^{-1} discharge capacity in a cut-off range between 2.5 and 4.6 V. It was found that the Al doping on $Li[Li_{0.15}Ni_{(0.275-x/2)}Al_xMn_{(0.575-x/2)}]O_2$ material could decrease the area specific impedance (ASI).

Keywords: Lithium-ion battery; Aluminum doping; Cathode materials; Layered structure; Manganese oxide

1. Introduction

At present, $LiCoO_2$ materials are the only commercially used cathode material in rechargeable lithium batteries. But $LiCoO_2$ has many problems, such as high cost and environmental disadvantages. Consequently, layered $LiMO_2$ (M = Ni, Mn) and spinel $LiMn_2O_4$ have been extensively researched for use as the cathode material for commercial lithium secondary batteries [1–3]. However, $LiNiO_2$ still has some severe problems, such as difficulty in the synthesis of stoichiometric $LiNiO_2$, capacity decay due to the formation of NiO_2 phases and thermal instability. Many researchers also have attempted to overcome these problems by substituting some other transition metals for Ni in $LiNiO_2$ to make $LiM_xNi_{1-x}O_2$ (M = Al, Co, Ga, Mg, Ti, etc.) [4–9]. Layered $LiMnO_2$ can be transformed into the cubic spinel structure through minor cationic rearrangements during the cycling, leading to degradation of electrode performance [10,11]. In order to stabilize the layered structure, many research groups have studied the Mn-substituted $Li_xM_yMn_{1-y}O_2$ (M = Al, Cr, Co, Ni, Li, Ti, Mg) [12–17]. Recently, Paulsen et al. [16] reported that high temperature O2-type $Li_{2/3}[Ni_{1/3}Mn_{2/3}]O_2$ was prepared by ion exchange from P2-type $Na_{2/3}[Ni_{1/3}Mn_{2/3}]O_2$.

Recently, many researchers have tried to make the solid solutions in the system of $LiNiO_2$ and $LiMnO_2$. Ohzuku and Makimura [18] reported that $Li(Ni_{0.5}Mn_{0.5})O_2$ materials are able to overcome the disadvantages of $LiNiO_2$ and $LiMnO_2$. Lu et al. [19] reported that $Li[Ni_xLi_{(1/3-2x/3)}Mn_{(2/3-x/3)}]$ is derived from Li_2MnO_3 or $Li[Li_{1/3}Mn_{2/3}]O_2$ by substitution of Li^+ and Mn^{4+} for Ni^{2+} while maintaining all the Mn ions in the 4+ oxidation state. Also, several researchers reported on the Li–Mn–Cr–O system [20,21]. These materials are solid solutions of Li_2MnO_3 and $LiCrO_2$, the electrochemical properties of which are derived from the oxidation of Cr ions ($Cr^{3+} \rightarrow Cr^{6+}$).

In this work, a sol–gel method was employed to prepare $Li[Li_{0.15}Ni_{(0.275-x/2)}Al_xMn_{(0.575-x/2)}]O_2$ ($x = 0$–0.1) powders using glycolic acid ($HOCH_2COOH$) as a chelating agent. The structural and electrochemical properties of the synthesized materials were investigated.

2. Experimental

Al-doped $Li[Li_{0.15}Ni_{(0.275-x/2)}Al_xMn_{(0.575-x/2)}]O_2$ ($x = 0$–0.1) powders were prepared using a sol–gel method. Lithium acetate ($Li(CH_3COO)\cdot 2H_2O$, Kanto Chemical Co.), aluminum nitrate ($Al(NO_3)_3\cdot 9H_2O$, Aldrich), manganese acetate ($Mn(CH_3COO)_2\cdot 4H_2O$, Acros Organics), and nickel acetate ($Ni(CH_3COO)_2\cdot 4H_2O$, Aldrich) salts were used as starting materials for the synthesis of $Li[Li_{0.15}Ni_{(0.275-x/2)}Al_x$-

* Corresponding author. Tel.: +82-2-2290-0524; fax: +82-2-2282-7329.
E-mail address: yksun@hanyang.ac.kr (Y.-K. Sun).

0378-7753/03/$ – see front matter © 2003 Elsevier Science B.V. All rights reserved.
doi:10.1016/S0378-7753(03)00171-X

$Mn_{(0.575-x/2)}]O_2$ powders. For $Li[Li_{0.15}Ni_{0.225}Al_{0.1}Mn_{0.525}]O_2$, for example, stoichiometric amounts of Li ($Li(CH_3COO)\cdot 2H_2O$), Al ($Al(NO_3)_3\cdot 9H_2O$), Mn ($Mn(CH_3COO)_2\cdot 4H_2O$), and Ni ($Ni(CH_3COO)_2\cdot 4H_2O$) salts (cationic ratio of Li:Al:Mn:Ni = 1.15:0.1:0.525:0.225) were dissolved in distilled water. The solution was added into a continuously agitated aqueous solution of glycolic acid ($HOCH_2COOH$, Kanto Chemical Co.), the chelating agent for the reaction. The molar ratio of glycolic acid to total metal ions was unity. The pH of the solution was adjusted in the range of 8–9 by adding ammonium hydroxide solution. The prepared solution was evaporated at 90 °C for several hours until a transparent sol was obtained. As the water evaporated further, the sol turns into a viscous transparent gel. The resulting gel precursors were heated at the rate of 5 °C min^{-1} and decomposed at 480 °C for 5 h in air to eliminate organic elements. The pre-calcinated powders were ground thoroughly for 30 min in an agate mortar before pelletizing. The pellets were calcined at 900 °C in air for 10 h, and then quenched to room temperature.

After the synthesis, powder X-ray diffraction (XRD, Rigaku) measurements using Cu Kα radiation were used to characterize the structures of the synthesized powders. Particle morphology of the powders after calcination was observed using a scanning electron microscope (SEM, JEOL, JSM 6400). Rietveld refinement was performed with the XRD data to obtain lattice parameters of the synthesized powders.

The electrochemical characterization was performed using CR2032 coin-type cells. This cell consisted of a cathode and a lithium metal anode (Cyprus Foote Mineral Co.) separated by a porous polyethylene film (Celgard 3401). The cathode was fabricated with 20 mg of accurately weighed active material and 12 mg of conductive binder (8 mg of teflonized acetylene black (TAB) and 4 mg of graphite). It was pressed onto a 20 mm^2 stainless steel mesh used as the current collector at 300 kg cm^{-2} and dried at 130 °C for 12 h in an vacuum oven in order to remove moisture. The electrolyte used was 1 M $LiPF_6$ in an ethylene carbonate–diethyl carbonate (EC–DEC, 1:1 by volume) solvent mixture. The cell was assembled in an argon-filled dry box and tested at room temperature (30 °C). The cell was charged and discharged at a current density of 0.4 mA cm^{-2} (C/4) with cut-off voltages of 2.5–4.6 V (versus Li/Li^+).

3. Results and discussion

Fig. 1 shows the XRD spectra for $Li[Li_{0.15}Ni_{(0.275-x/2)}Al_xMn_{(0.575-x/2)}]O_2$ ($x = 0$–0.1) powders. The XRD spectra show that the prepared samples have the typical hexagonal layered structure ($R\bar{3}m$) and a minor amount of Li_2MnO_3 monoclinic phase. The peak near 21° appears to be characteristic of the Li_2MnO_3 monoclinic structure, which would result from the random stacking of the ordered layers [19]. No other impurity-related peaks are observed in the

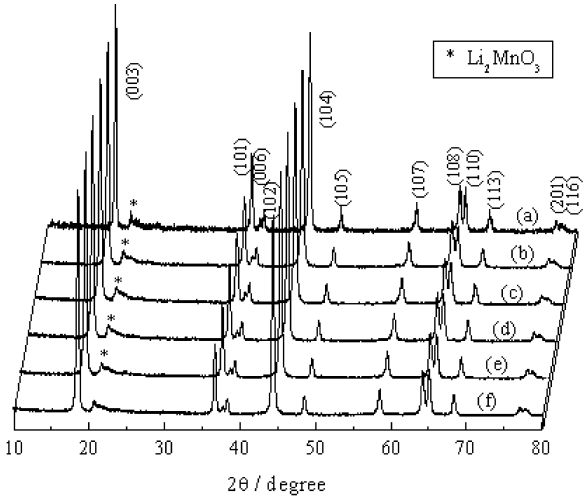

Fig. 1. The X-ray diffraction patterns for $Li[Li_{0.15}Ni_{(0.275-x/2)}Al_xMn_{(0.575-x/2)}]O_2$ powder prepared at various aluminum contents, x in (a) 0, (b) 0.02, (c) 0.04, (d) 0.06, (e) 0.08, and (f) 0.1.

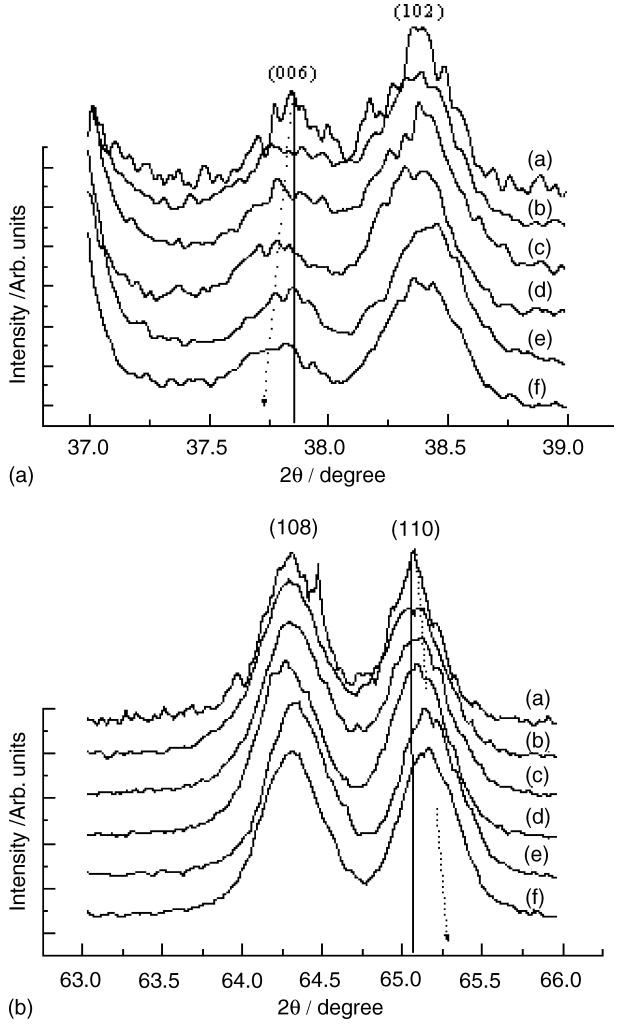

Fig. 2. The X-ray diffraction patterns for peak split condition of (a) (0 0 6)/(1 0 2), and (b) (1 0 8)/(1 1 0) directions, prepared at various aluminum contents, x in (a) 0, (b) 0.02, (c) 0.04, (d) 0.06, (e) 0.08, and (f) 0.1.

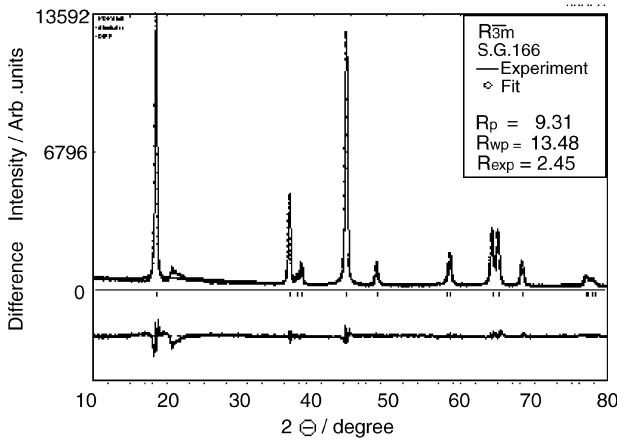

Fig. 3. Rietveld refinements to the diffraction pattern of $Li[Li_{0.15}Ni_{(0.275-x/2)}Al_xMn_{(0.575-x/2)}]O_2$ with $x = 0.06$. The calculated patterns are based on the $LiNiO_2$ structure ($R\bar{3}m$).

XRD spectrum of $Li[Li_{0.15}Ni_{(0.275-x/2)}Al_xMn_{(0.575-x/2)}]O_2$ powders with increasing aluminum doping contents. These results indicate that the Al ions can substitute for Ni and Mn at the 3a site. Fig. 2(a) and (b) shows that the (0 0 6) peak shifts toward lower diffraction angles and the (1 1 0) peak shifts toward higher diffraction angles as the aluminum content increases. The transition of these diffraction angles results in a clear split of the (0 0 6)(1 0 2) and (1 0 8)(1 1 0) directions. These phenomena can be explained by the fact that the Al^{3+} ion substituted into the 3a site generates a microscopic stress in the basal plane of the $R\bar{3}m$ structure [22]. All of the full width half maximum (FWHM) of all the peaks become wider with the increase of aluminum content, which suggests a microscopic strain due to mismatch of Al^{3+}, Ni^{2+} and Mn^{4+} ions. Fig. 3 shows the XRD patterns of $Li[Li_{0.15}Ni_{(0.275-x/2)}Al_xMn_{(0.575-x/2)}O_2$ ($x = 0.06$) and the calculated pattern based on the best Rietveld refinement. Except for the 22° Li_2MnO_3 superlattice peaks, the entire XRD pattern is well fitted by the same structure model as O3–$LiNiO_2$ hexagonal structure. Small differences between

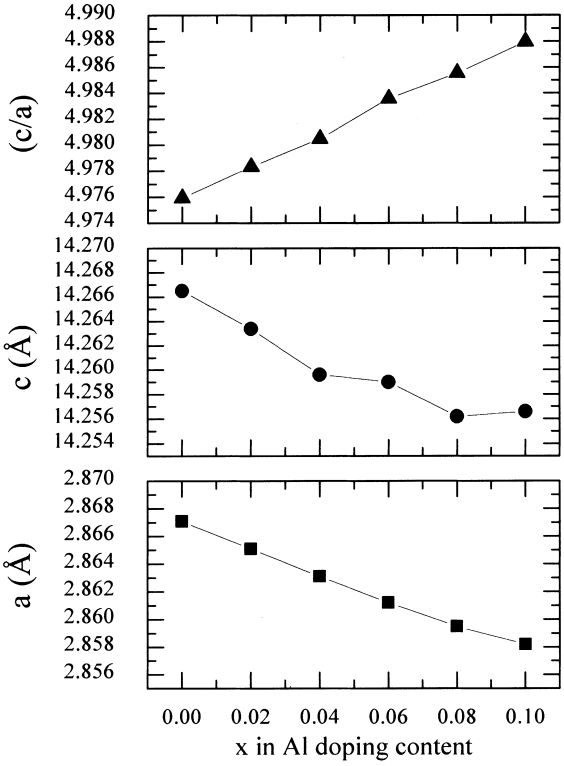

Fig. 4. The lattice constants a, c, and the c/a ratio vs. x in $Li[Li_{0.15}Ni_{(0.275-x/2)}Al_xMn_{(0.575-x/2)}]O_2$ powder.

both intensities and R_{wp} of 12.67–13.79% would show a successful refinement [23]. The lattice constants, a, c, and c/a ratios of $Li[Li_{0.15}Ni_{(0.275-x/2)}Al_xMn_{(0.575-x/2)}]O_2$ were calculated by the Rietveld refinement method using the XRD data and are presented in Fig. 4. As the aluminum content increases, the lattice constant a and c decreases from 2.8671 to 2.8582, and 14.2665 to 14.2566 Å, respectively. The decrease of a and c is because the ionic size of Al^{3+} (0.535 Å) is smaller than that of Ni^{2+} (0.69 Å) and similar to Mn^{+4} (0.53 Å). The c/a ratios are over 4.97, indicating the hexagonal phase for all aluminum contents.

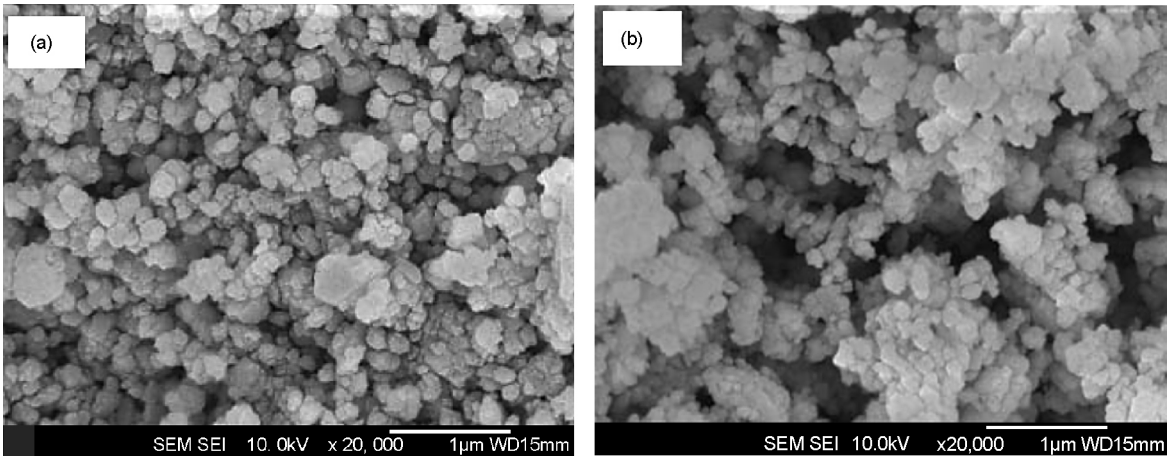

Fig. 5. Scanning electron micrographs for $Li[Li_{0.15}Ni_{(0.275-x/2)}Al_xMn_{(0.575-x/2)}]O_2$ powder: (a) $x = 0$, (b) $x = 0.06$.

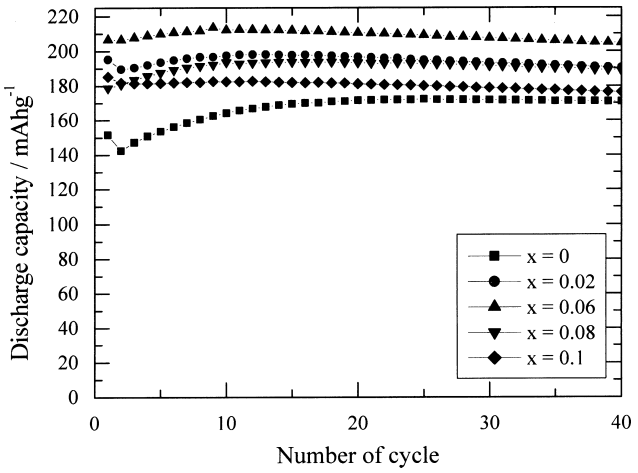

Fig. 6. Plots of specific discharge capacity vs. number of cycles for the various aluminum contents in $Li[Li_{0.15}Ni_{(0.275-x/2)}Al_xMn_{(0.575-x/2)}]O_2$ powder.

Fig. 5(a) and (b) show the SEM photographs for $Li[Li_{0.15}Ni_{(0.275-x/2)}Al_xMn_{(0.575-x/2)}]O_2$ ($x = 0.06$) and undoped powders, respectively. The average particle size is about 50–200 nm. All prepared samples have a spherical shape. It was concluded that the aluminum doping did not influence powder morphology.

Fig. 6 shows plots of the discharge capacity measured at room temperature as a function of the cycle number for $Li[Li_{0.15}Ni_{(0.275-x/2)}Al_xMn_{(0.575-x/2)}]O_2$ ($x = 0$–0.1) electrodes. The cells were tested under a constant charge–discharge current density of 0.4 mA cm^{-2} (C/4) between 2.5 and 4.6 V. The $Li[Li_{0.15}Ni_{0.275}Mn_{0.575}]O_2$ electrodes delivered initial discharge capacities of 150 mAh g^{-1}, which increased steadily on subsequent cycling. However, aluminum doped $Li[Li_{0.15}Ni_{(0.275-x/2)}Al_xMn_{(0.575-x/2)}]O_2$ electrodes showed higher capacity than undoped electrodes, with excellent cyclability.

Fig. 7(a) and (b) shows the charge–discharge curves of $Li[Li_{0.15}Ni_{(0.275-x/2)}Al_xMn_{(0.575-x/2)}]O_2$ electrodes ($x = 0$ and 0.06). The reversible specific capacity of $Li[Li_{0.15}Ni_{0.245}Mn_{0.545}]O_2$ was 160 mAh g^{-1}, and that of the 6 mol% aluminum-doped sample was around 210 mAh g^{-1}. However, the first irreversible charge capacity (over 4.45 V) of the Al doped sample was greater than in the undoped sample. This irreversible charge capacity (plateau) was already reported by Lu and Dahn [24]. They suggested that expelled oxygen causes this anomalous plateau. However, at present we do not clearly understand this phenomenon.

Fig. 8 shows the differential capacity versus voltage of $Li[Li_{0.15}Ni_{(0.275-x/2)}Al_xMn_{(0.575-x/2)}]O_2$ ($x = 0$, 0.06, and 0.1) electrodes first cycled between 2.5 and 4.6 V. In the charge, the oxidation peaks at 4.5 V of $Li[Li_{0.15}Ni_{(0.275-x/2)}Al_xMn_{(0.575-x/2)}]O_2$ electrodes were strikingly different than other oxidation peaks. The drastic oxidation peak (4.5 V) correspond to the plateau as shown in Fig. 7. These peaks suggest that two single phases are sandwiched, one phase below 4.4 V and another above 4.5 V. However, the differential

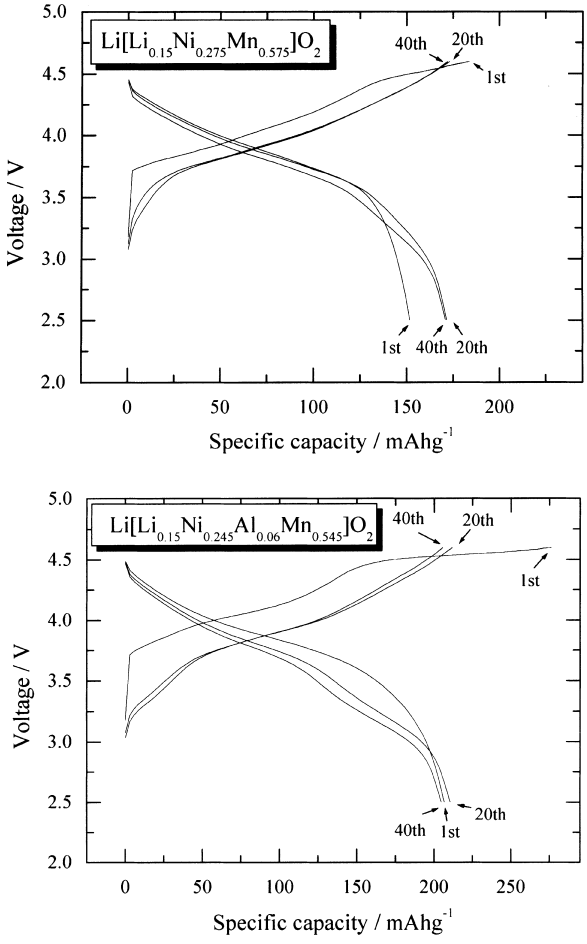

Fig. 7. Specific capacity vs. voltage curves for $Li[Li_{0.15}Ni_{(0.275-x/2)}Al_xMn_{(0.575-x/2)}]O_2$ powders ($x = 0$, and 0.06).

capacity versus voltage curve of the aluminum doped electrode is different from that of the undoped sample. The undoped electrode has three oxidation peaks at 3.8, 4.05, and 4.5 V. These results indicate four-stepped structural

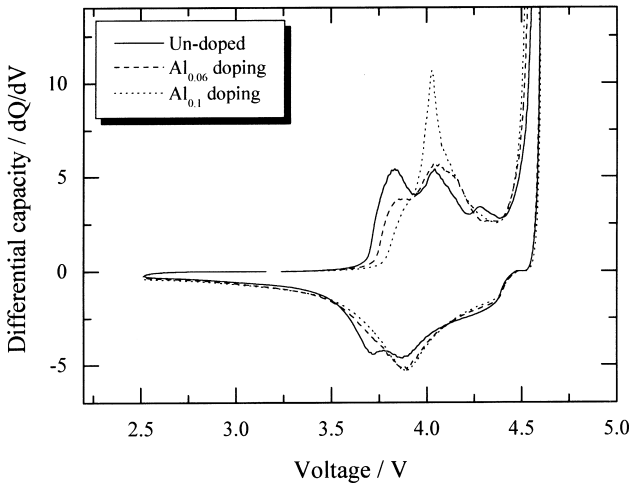

Fig. 8. Differential capacity vs. voltage for $Li/Li[Li_{0.15}Ni_{(0.275-x/2)}Al_xMn_{(0.575-x/2)}]O_2$ cells. The cells were charged–discharge between 2.5 and 4.6 V using a specific current of 0.4 mA cm^{-2} (C/4).

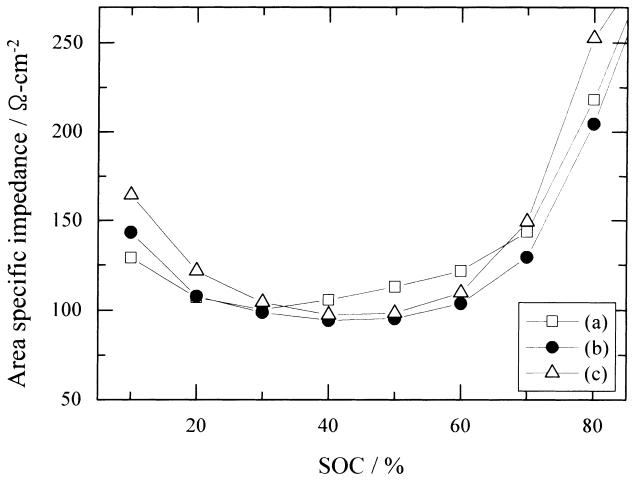

Fig. 9. Area specific impedance (ASI) vs. state of charge (SOC) for $Li[Li_{0.15}Ni_{(0.275-x/2)}Al_xMn_{(0.575-x/2)}]O_2$ electrode: (a) $x = 0$, (b) $x = 0.06$, and (c) $x = 0.1$.

changes in the charge process. Meanwhile, for the Al doped sample, the oxidation peak at 3.8 V disappears at 4.05 V oxidation peak increase with increased Al content. The observation of a monotonous curve indicates that the doped aluminum ion enhances the structural stability, because the bonding energy of Al–O bonds (512 kJ mol^{-1}) is higher than that of Ni–O bonds (391.6 kJ mol^{-1}) or Mn–O bonds (402.34 kJ mol^{-1}) [25].

Area specific impedance (ASI) indicates the power capability of a battery performance. During the lithium intercalation–de-intercalation processes, a combination of electrode polarization, Ohmic drop, Li^+ ion diffusion through the electrolyte, and solid-state lithium ion diffusion within the electrode cause the overall cell voltage to change [26]. Fig. 9 shows the ASI as a function of state of charge (SOC) measured with $Li/Li[Li_{0.15}Ni_{(0.275-x/2)}Al_xMn_{(0.575-x/2)}O_2$ ($x = 0$, 0.06, and 0.1) cells. The ASI was determined by $A{\cdot}\Delta V/I$, where A is the cross-sectional area (2.0 cm^2), ΔV the voltage drop during current interruption (V_2–V_1) for 60 s at each SOC, and I the constant current applied during the galvanostatic cycling. The 6 mol% aluminum doping on $Li/Li[Li_{0.15}Ni_{(0.275-x/2)}Al_xMn_{(0.575-x/2)}O_2$ cell exhibited a smaller ASI value than the undoped sample. It is speculated that partly Al doped materials have a faster chemical diffusion than undoped materials in lithium ion batteries.

4. Conclusion

Layered $Li[Li_{0.15}Ni_{(0.275-x/2)}Al_xMn_{(0.575-x/2)}]O_2$ ($x =$ 0–0.1) materials were synthesized using a sol–gel method. The $Li[Li_{0.15}Ni_{0.275}Mn_{0.575}O_2$ material delivered a discharge capacity of 150 mAh g^{-1} between 2.5–4.6 V. However, 6 mol% aluminum doped of $Li[Li_{0.15}Ni_{(0.275-x/2)}Al_x$-$Mn_{(0.575-x/2)}O_2$ materials delivered a discharge capacity of 210 mAh g^{-1} and good capacity retention. The area specific impedance (ASI) was determined by $A{\cdot}\Delta V/I$ at each SOC. The 6 mol% Al^{3+} doped material showed decreased area specific impedance (ASI) when compared to the undoped sample.

Acknowledgements

This work was supported by KOSEF through the Research Centre for Energy Conversion and Storage.

References

[1] G. Dutta, A. Manthiram, J.B. Goodenough, J. Solid State Chem. 96 (1992) 123.
[2] A.R. Armstrong, P.G. Bruce, Nature 381 (1996) 499.
[3] T. Ohzuku, A. Ueda, M. Nagayama, J. Electrochem. Soc. 140 (1993) 1862.
[4] T. Ohzuku, T. Yanagawa, M. Kouguchi, A. Ueda, J. Power Sources 68 (1997) 131.
[5] Y. Nitta, K. Okamura, K. Haraguchi, S. Kobayashi, A. Ohta, J. Power Sources 54 (1995) 511.
[6] B. Banov, J. Bourilkov, M. Mladenov, J. Power Sources 54 (1995) 268.
[7] Y. Nishida, K. Nakane, T. Satoh, J. Power Sources 68 (1997) 561.
[8] H. Arai, S. Okada, Y. Sakurai, J. Yamaki, J. Electrochem. Soc. 144 (1997) 3117.
[9] Y. Gao, M.V. Yakovleva, W.B. Ebner, Electrochem. Solid State Lett. 1 (3) (1998) 117.
[10] G. Vitins, K. West, J. Electrochem. Soc. 144 (1997) 2587.
[11] Y.-I. Jang, B. Huang, Y.-M. Ching, D.R. Sadoway, Electrochem. Solid State Lett. 1 (1998) 13.
[12] I.J. Davidson, R.J. Mcllan, J.J. Murray, J.E. Greedan, J. Power Sources 54 (1995) 232.
[13] L. Croguennec, P. Deniard, R. Brec, J. Electrochem. Soc. 144 (1997) 3323.
[14] M.E. Spahr, P. Novak, O. Haas, R. Nesper, J. Power Sources 68 (1997) 629.
[15] J.M. Paulsen, R.A. Donaberger, J.R. Dahn, Chem. Mater. 12 (2000) 2257.
[16] J.M. Paulsen, C.L. Thomas, J.R. Dahn, J. Electrochem. Soc. 146 (1999) 3560.
[17] J.P. Parant, R. Olazcuaga, M. Devalette, C. Fouassier, P. Hagenmuller, J. Solid Chem. 3 (1971) 1.
[18] T. Ohzuku, in: Proceedings of the 11th International Meeting on Lithium Batteries (IMLB), Monterey, USA, June 2002 (Abstract 11).
[19] Z. Lu, D.D. MacNeil, J.R. Dahn, Electrochem. Solid State Lett. 4 (2001) A191.
[20] J.M. Paulsen, B. Ammundsen, H. Desilvestro, R. Steiner, D. Hassll, in: Proceedings of the Tenth International Meeting on Lithium Batteries (IMLB), Como, Italy, May 2000 (Abstract 71).
[21] J. Cho, Y.J. Kim, B. Park, Solid State Ion. 138 (2001) 221.
[22] T. Ohzuku, A. Ueda, M. Kouguchi, J. Electrochem. Soc. 142 (1995) 4033.
[23] F. Lzumi, Nippon Kessho Gakkai Shi. 27 (1985) 23.
[24] Z. Lu, J.R. Dahn, J. Electrochem. Soc. 149 (7) (2002) A815.
[25] J.A Dean, Lange's Handbook of Chemistry, 4th ed., McGraw-Hill, New York, 1992, p. s.4.
[26] Q. Wu, W. Lu, J. Prakash, J. Power Sources 88 (2000) 237.